photonics

MDPI

Article

Toroidal Dipole Excitation in Metamaterial Perfect Absorber Consisting of Dielectric Nanodisks Quadrumer Clusters and Spacer on Metal Substrate

Yuepei Cai, Yong Huang and Keyong Zhu *

School of Aeronautic Science and Engineering, Beihang University, Beijing 100191, China; caiyuepei@buaa.edu.cn (Y.C.); huangy@buaa.edu.cn (Y.H.)
* Correspondence: zhukeyong@buaa.edu.cn

Abstract: We proposed an infrared narrowband metamaterial perfect absorber (MPA) which is induced by toroidal dipole resonance in a dielectric-metal hybrid system. The MPA is composed of amorphous-silicon (a-Si) nanodisk quadrumer clusters, dielectric spacer, and Au substrate, where the dielectric spacer is inserted between Si disk quadrumer and Au substrate. Near field distribution and multipole decomposition of far-field, scattering powers show that toroidal dipole mode is formed by opposite phase magnetic dipoles in neighboring Si nanodisks. The effects of geometric and material parameters on absorption characteristics were explored. The sensing performance of the MPA was also evaluated. The proposed MPA has potential applications in air sensing applications. Since the nanodisks quadrumer of the MPA retains C_{4v} symmetry, perfect absorption band is polarization independent. Furthermore, the absorption quality factor of the hybrid dielectric-metal hybrid absorber is higher than that of all-metal perfect absorbers, thanks to the low loss feature of the dielectric resonator.

Keywords: metamaterial perfect absorber; toroidal dipole resonance; gas sensing

Citation: Cai, Y.; Huang, Y.; Zhu, K. Toroidal Dipole Excitation in Metamaterial Perfect Absorber Consisting of Dielectric Nanodisks Quadrumer Clusters and Spacer on Metal Substrate. *Photonics* **2022**, *9*, 462. https://doi.org/10.3390/photonics9070462

Received: 13 June 2022
Accepted: 27 June 2022
Published: 30 June 2022

1. Introduction

Metamaterial perfect absorbers (MPA), which are artificial material structures usually periodically arranged, i.e., metamaterial, that can absorb incident electromagnetic waves totally or near totally at the designed wavelength [1]. MPAs can find promising applications in many regions including thermophotovoltaics [2,3], infrared stealth [4,5], radiative cooling [6,7], infrared photodetectors [8,9], sensors [10–13], and modulators [14,15] up to date since the first MPA was demonstrated in microwave frequency [16]. Physical mechanism to design MPA's perfect absorption can usually be attributed to electromagnetic resonance including electric and magnetic multipoles [17–19], coupling effects between multipoles [20], and critical coupling in the bound states in the continuum [21]. Recently, a new kind of resonance dominated by toroidal dipole has attracted considerable and growing attention owing to it violates both the space-inversion and time-reversal symmetries [22], which may facilitate to design new kind of MPA.

Toroidal dipole results from poloidal currents flowing on the torus surface along its meridians with the characterization of a closed head-to-tail magnetic loop [23]. Toroidal dipole is usually overlooked in the natural medium due to a much weaker electromagnetic response compared with electric and magnetic multipoles [24]. Fortunately, toroidal dipole response can be greatly enhanced in metamaterials [25]. As a demonstration, a structure comprising of a 3D array of toroidal solenoids was firstly proved numerically in 2007 [26]. Experimental observations were taken from microwave region [24] to optical frequency [27] utilizing a subwavelength four asymmetric split ring (SRR) resonators array. Since subwavelength SRRs are not easy to fabricate especially in the optical region, a simple structure which supports magnetic resonances including plasmonic cavities [28],

Metal/Dielectric/Metal structure [29] and high refractive index dielectric particle [30] were used to construct toroidal dipole resonators. Considering that all dielectric metasurfaces consisting of high refractive index dielectric particles ire easy to fabricate and has low intrinsic losses, all dielectric metasurfaces that support toroidal dipole have intrigued great attention in research about the response enhancement of toroidal dipole [31,32].

MPAs which support toroidal dipole were proposed utilizing different kinds of resonators including L-shaped metal strip [33], depth asymmetry metallic circular groove [34], and C-shaped groove array [35]. However, most of them suffer from low quality factors and polarization dependence, which is not desired for sensing application. Dielectric-metal hybrid systems are promising in designing narrow band MPAs since their bandwidth is often narrow [36,37]. Inspired by the aforementioned all dielectric metasurface which supports toroidal dipole resonance and narrow band perfect absorption in a dielectric-plasmonic system, we proposed a dielectric-metal hybrid metamaterial narrowband toroidal dipole induced perfect absorber consisting of Si disks quadrumer clusters and dielectric spacer on a metal substrate in a near-infrared wavelength range. It is found that toroidal dipole is caused by the coupling effect of magnetic dipole with opposite phase in neighboring Si nanodisks. Toroidal dipole resonance can be excited under arbitrary polarization angle at normal incidence conditions. Geometric parameters on toroidal dipole resonance perfect absorption were also studied in detail. Considering its narrow bandwidth and sensitivity to environmental medium, the performance of the proposed MPA in refractive index sensing application was also discussed.

2. Model and Method

The designed MPA is composed of amorphous-Silicon (a-Si) nanodisk quadrumer clusters, plasma-deposited Silicon Nitride (SiNx) spacer and Au substrate from top to bottom as shown in Figure 1. To keep forth-fold symmetry, the MPA is arranged periodically in both x and y directions with the same geometric parameters. Quadrumer is composed of four squarely distributed disks with diameter d and height h. The gaps between neighboring disks along x or y direction in a unit cell are labeled as g. The thickness of dielectric spacer and metal substrate are set as t_1 and t_2, respectively. The permittivity of Au is modeled by Drude equation with plasma frequency $\omega_p = 1.37 \times 10^{16}$ rad/s and collision frequency $\gamma = 7.31 \times 10^{13}$ rad/s [38]. The refractive index of SiNx spacer and a-Si were set as 2 [39] and 3.42 [40]. Unless otherwise specified, the geometric parameters are set as p = 1110 nm, d = 464 nm, h = 232 nm, g = 55 nm, t_1 = 38 nm and t_2 = 400 nm.

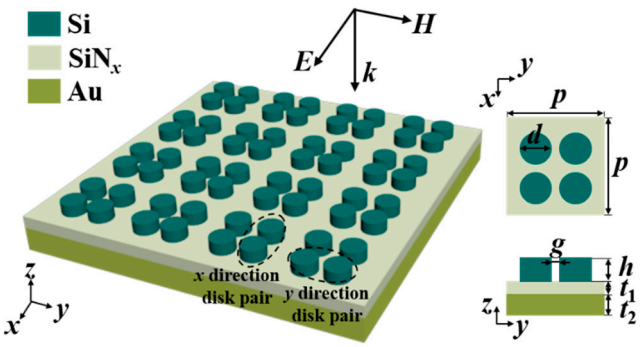

Figure 1. Schematic view of the MPA and its unit cell.

Absorption spectra and electromagnetic field distribution are calculated by COMSOL Multiphysics. Single unit cell is simulated with periodic condition applied in x and y directions. Perfect matched layer condition is applied in z direction above the MPA distance about one-half of maximum wavelength. Since thickness of Au substrate is thick enough to prevent light from transmitting, the absorption A of whole structure can be obtained with $A = 1 - R$ with R representing the reflection. Multipolar decomposition of scattered

powers is performed in Cartesian coordinate system using Equations (1)–(11) to clarify the resonance contribution [29].

$$\boldsymbol{J} = i\omega\varepsilon_0(\varepsilon_a - \varepsilon_b)\boldsymbol{E}_{(r)} \tag{1}$$

$$\boldsymbol{p} = \frac{i}{\omega}\int \boldsymbol{J}\mathrm{d}^3 r \tag{2}$$

$$\boldsymbol{m} = \frac{1}{2}\int (\boldsymbol{r}\times\boldsymbol{J})\mathrm{d}^3 r \tag{3}$$

$$\boldsymbol{t} = \frac{1}{10}\int \left[(\boldsymbol{r}\cdot\boldsymbol{J})\boldsymbol{r} - 2\boldsymbol{r}^2\boldsymbol{J}\right]\mathrm{d}^3 r \tag{4}$$

$$\boldsymbol{eq}_{\alpha\beta} = \frac{i}{\omega}\int \left[\boldsymbol{r}_\alpha\boldsymbol{J}_\beta + \boldsymbol{r}_\beta\boldsymbol{J}_\alpha - \frac{2}{3}\delta_{\alpha,\beta}(\boldsymbol{r}\cdot\boldsymbol{J})\right]\mathrm{d}^3 r \tag{5}$$

$$\boldsymbol{mq}_{\alpha\beta} = \frac{1}{3}\int \left[(\boldsymbol{r}\times\boldsymbol{J})_\alpha\boldsymbol{r}_\beta + (\boldsymbol{r}\times\boldsymbol{J})_\beta\boldsymbol{r}_\alpha\right]\mathrm{d}^3 r \tag{6}$$

$$I_p = \frac{2\omega^4}{3c^3}|\boldsymbol{p}|^2 \tag{7}$$

$$I_m = \frac{2\omega^4}{3c^3}|\boldsymbol{m}|^2 \tag{8}$$

$$I_t = \frac{2\omega^4}{3c^5}|\boldsymbol{t}|^2 \tag{9}$$

$$I_{eq} = \frac{\omega^6}{5c^5}\Sigma\left|\boldsymbol{eq}_{\alpha\beta}\right|^2 \tag{10}$$

$$I_{mq} = \frac{\omega^6}{40c^5}\Sigma\left|\boldsymbol{mq}_{\alpha\beta}\right|^2 \tag{11}$$

where $\boldsymbol{J}$ is the induced polarization current density, $\boldsymbol{r}$ is the position vector, ω is the circular frequency of incident wave, ε_a is the permittivity of corresponding material in MPA, ε_b is the permittivity of surrounding background medium and c is the speed of light in background medium. Dipole moments and quadrupole moments including electric dipole $\boldsymbol{p}$, magnetic dipole $\boldsymbol{m}$, toroidal dipole $\boldsymbol{t}$, electric quadrupole $\boldsymbol{eq}$, magnetic quadrupole $\boldsymbol{mq}$ are derived by integral the vector operation of $\boldsymbol{r}$ and $\boldsymbol{J}$ over a unit cell as described by Equations (2)–(6), and the subscripts α, $\beta = x, y$ or z. The scattered power I_p, I_m, I_t, I_{eq} and I_{mq} are calculated from $\boldsymbol{p}$, $\boldsymbol{m}$, $\boldsymbol{t}$, $\boldsymbol{eq}$ and $\boldsymbol{mq}$ by Equations (7)–(11).

3. Results and Discussion

Figure 2 depicts the absorption spectra (black solid line) of our designed MPA when the structure is impinged by x polarized light at normal incidence conditions. In fact, the absorption spectra at y polarized light normal incidence condition overlap with the black solid line which can attribute to the structure's 90° rotational symmetry. Resonance absorption can be found at an optical communication wavelength 1550 nm with A larger than 0.99, and full width at half maximum (FWHM) about 5 nm. To understand the perfect absorption mechanism at 1550 nm, coupled mode theory (CMT) was used to describe the absorption spectrum theoretically [41,42]. According to CMT, the reflection coefficient r of single-port system as an analog of the MPA can be expressed as

$$r = \frac{s_-}{s_+} = \frac{\gamma_e - \gamma_i + j(\omega - \omega_0)}{\gamma_e + \gamma_i + j(\omega - \omega_0)} \tag{12}$$

where s_- and s_+ represent the output and input waves of amplitudes respectively. γ_e and γ_i are external leakage rate and intrinsic loss rate of the MPA respectively. ω_0 is resonance circular frequency. Absorption $A = 1 - |r|^2$ thus A can be expressed as

$$A = \frac{4\gamma_e\gamma_i}{(\omega - \omega_0)^2 + (\gamma_e + \gamma_i)^2} \tag{13}$$

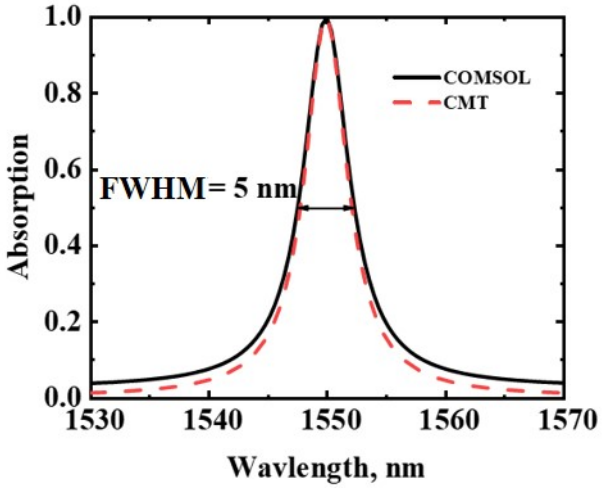

Figure 2. Absorption spectra of the MPA for *x*-polarized light at normal incidence condition.

When the MPA is driven on resonance ($\omega = \omega_0$), and the external leakage and intrinsic loss rates are the same ($\gamma_e = \gamma_i$), A equals to 1 which means critical coupling states is fulfilled, and all incident energy can be absorbed totally. The Equation (13) is used to fit the COMSOL calculated absorption spectrum, and they fit well with each other, as shown in Figure 2. Fitting parameters are: $\omega_0 = 1.26 \times 10^{15}$ rad/s and $\gamma_e = \gamma_i = 4.05 \times 10^{12}$ rad/s respectively.

To gain deep insight into the physical mechanism of resonance absorption, we plot the scattering powers of different multipoles in a Cartesian coordinate system in Figure 3. It can be observed clearly that the contribution of toroidal dipole moment is dominated at resonance wavelength 1550 nm which indicates the resonance absorption is mainly induced by toroidal dipole in Figure 3a. Simultaneously, magnetic quadruple ***mq*** also provides a noticeable contribution which is consistent with previous study [39,40]. By decomposing the *x*, *y* and *z* components of scattered power in Figure 3b–d, we find that the *x* component of scatter power from toroidal dipole $I_{t,x}$ is predominant in toroidal dipole scattered power and nearly equals to it in value, whereas *y* and *z* components of scatter power from toroidal dipole, $I_{t,y}$ and $I_{t,z}$ approach zero compared to $I_{t,x}$. This indicates the toroidal dipole moment is along the *x*-direction when the MPA is illuminated by *x* polarized light.

To further demonstrate the absorption peak is induced by toroidal dipole resonance, we plot the electromagnetic field of the MPA at resonance absorption peak wavelength in Figure 4. The black solid lines sketch the geometry of the MPA's unit cell. Figure 4a depicts the magnetic field distribution of the nanodisks quadrumer at *x*-*y* plane with black cones represent the displacement current. It can be observed clearly that, circulation orientations of displacement currents in *y* direction a-Si neighboring disks are opposite, and the same in *x*-direction a-Si neighboring disks, which indicates opposite phase magnetic dipoles along the z-direction were induced in *y*-direction disks pair. Figure 4b depicts the magnetic field distribution at the *y*-*z* plane with black arrows representing the magnetic field vector. Opposite magnetic dipoles caused a closed magnetic vortex in the *y*-*z* plane. Magnetic field vector distributed in a head-to-tail manner, which is the characterization of toroidal dipole resonance, and the direction of toroidal dipole moment is along *x*-direction according to the right-hand screw rule. Electromagnetic power is mainly dissipated between two *y*-direction coupled neighboring a-Si disk pairs, while no coupling effect caused power dissipation in *x*-direction as shown in Figure 4c,d. This also indicates that resonant absorption is induced by opposite phase magnetic dipole in *y*-direction a-Si disk pairs, which we name as toroidal dipole resonance as aforementioned. Also, the toroidal dipole resonance

electromagnetic field enhancement is mainly located at lossless Si nanodisks rather than lossy metal substrate, and this is the mechanism of narrow absorption bandwidth.

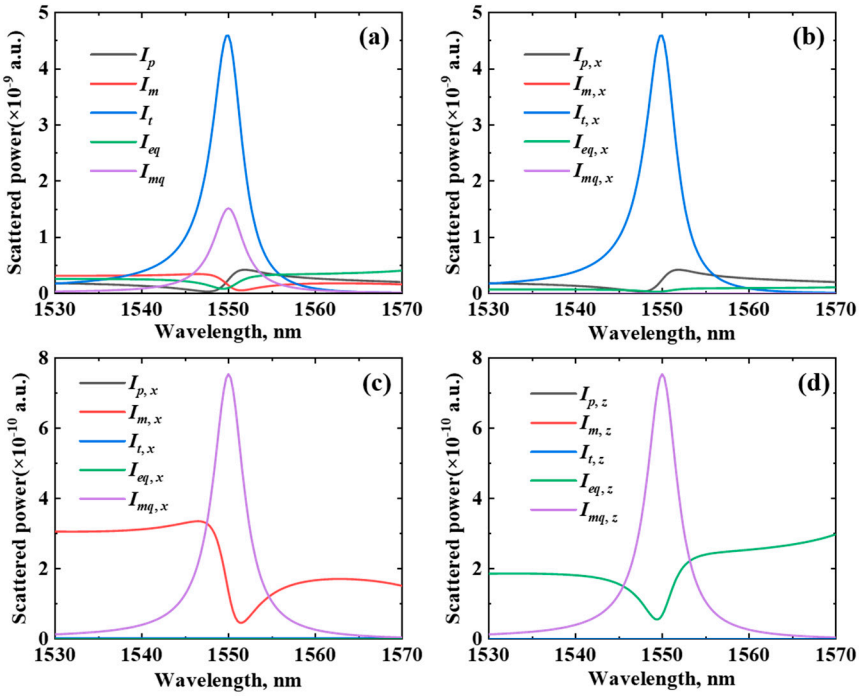

Figure 3. (**a**) Scattered powers from multipoles in terms of electric dipole (***p***, black solid line), magnetic dipole (***m***, red solid line), toroidal dipole (***t***, blue solid line), electric quadruple (***eq***, green solid line) and magnetic quadruple (***mq***, purple solid line). (**b**–**d**) *x*, *y* and *z* component of scatter powers respectively.

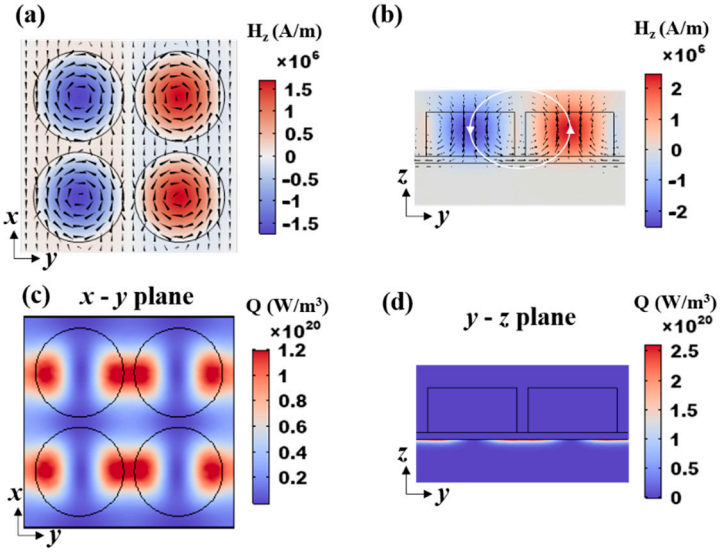

Figure 4. Electromagnetic field distribution at resonant wavelength. (**a**) Magnetic field distribution in *x* – *y* plane. Black cones represent the displacement current. (**b**) Magnetic field distribution in *y* – *z* plane. Black arrows denote the magnetic field vector. (**c**) Electromagnetic power dispassion density distribution in *x* – *y* plane and (**d**) *y* – *z* plane.

Most toroidal dipole resonance induced perfect absorption in MPAs are sensitive to polarization state. Our proposed MPA has the attractive property of being polarization-independent at normal incidence condition which can attribute to its 90° rotational symmetry. As shown in Figure 5a, the shape of absorption spectra under polarization angle

from 15° to 75° are almost the same as absorption spectra under x polarized incidence condition with nearly unchanged resonance wavelength. While the direction of toroidal dipole moment is polarization-dependent. When the polarization angle increases from 15° to 75°, $I_{t,x}$ (solid line) increases and $I_{t,y}$ (dotted line) decreases gradually as depicted in Figure 5b, which indicates the direction of $\boldsymbol{t}$ shifts from x-direction to y-direction gradually. Since $I_{t,z}$ (dashed line) nearly approaches to 0 compared with $I_{t,x}$ and $I_{t,y}$, direction angle θ_t of $\boldsymbol{t}$ be obtained by $\theta_t = \mathrm{atan}(\boldsymbol{t}_y/\boldsymbol{t}_x) = \mathrm{atan}(\sqrt{I_{t,x}/I_{t,y}})$. As shown in Figure 5c, the slope of linear fit line nearly equals 1 which indicates the direction of toroidal dipole moment is parallel to polarization direction at resonance wavelength.

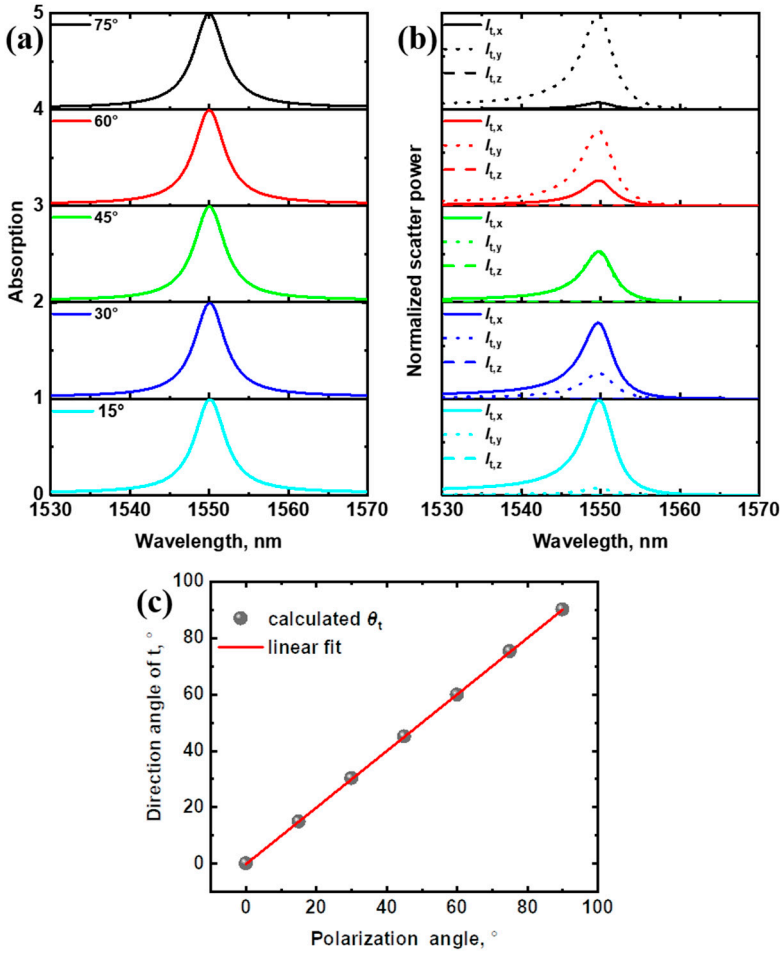

Figure 5. (**a**) Absorption spectra of the MPA for polarization angle from 15° to 75° with a step interval of 15°. (**b**) Normalized scatter power of $\boldsymbol{t}$. (**c**) Linear fitting of θ_t at resonant wavelength as a function of polarization angle.

The effects of geometric parameters on the resonance absorption of the proposed MPA is also investigated respectively. As shown in Figure 6a,b increasing p or g causes a blueshift of resonant wavelength. Both p and g have influence on the coupling strength on neighboring Mie resonators thus when p or g were changed from critical coupled state, resonance absorption would be weakened [43]. The difference is that increasing p causes resonant state changing from under coupling state ($\gamma_i > \gamma_e$) to critical coupling state ($\gamma_i = \gamma_e$) and then to over coupling state ($\gamma_i < \gamma_e$) successively, whereas increasing g causes resonant state changing from over coupling state ($\gamma_i < \gamma_e$) to critical coupling state ($\gamma_i = \gamma_e$) and then to under coupling state ($\gamma_i > \gamma_e$) successively [44]. The resonant wavelength position is also sensitive to the height h and diameter d of Si nanodisks, because the electromagnetic scattering property of Si nanodisks is governed by the Mie resonance. In sphere Mie resonators, magnetic dipole resonance wavelength is proportional to its radius. Increasing

h or *d* of nanodisks is equal to increasing the radius of its equivalent sphere Mie resonator thus causing a redshift of resonance wavelength as shown in Figure 6c,d.

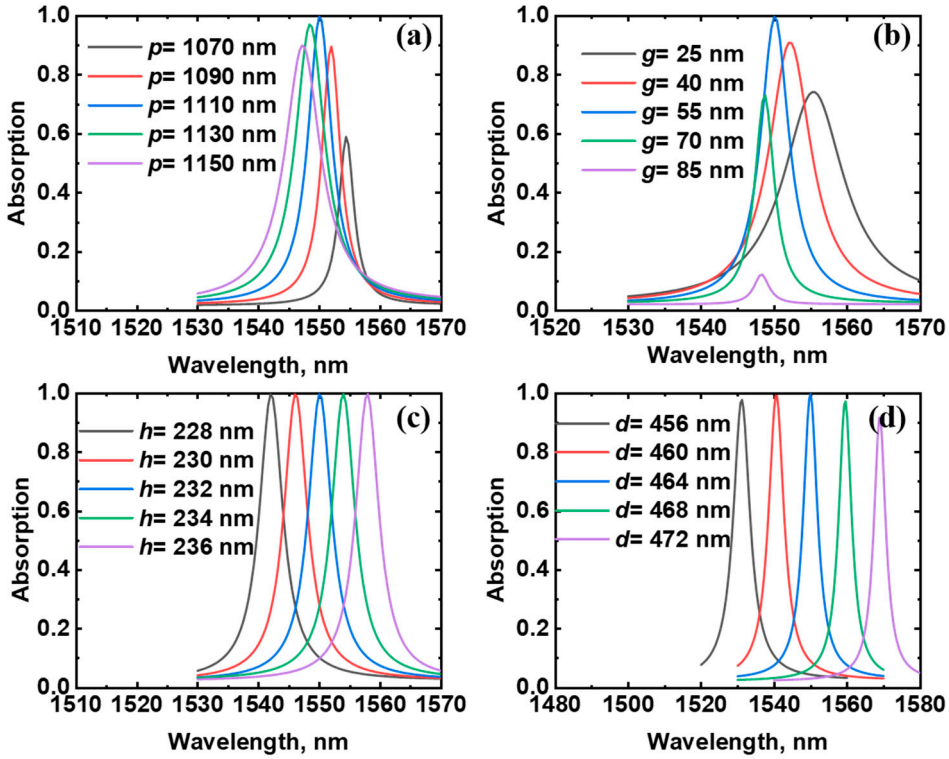

Figure 6. Absorption spectra for various geometrical parameters: (**a**) period *p*, (**b**) gap distance *g*, (**c**) thickness of a-Si disk *h* and (**d**) diameter of a-Si disk *d*.

The resonance absorption wavelength can also be tuned by the spacer's refractive index and thickness since the dielectric spacer affects the coupling between nanodisk resonators and metal substrate [45]. As shown in Figure 7a, λ_r redshifts occur from 1542 nm to 1559 nm when increasing the refractive index of dielectric spacer ns from 1.5 to 2.5. This can be understood by the perturbation theory that $(\Delta\omega/\omega) = -(\int\int\int \Delta\varepsilon |E|^2 dV / 2\int\int\int \varepsilon |E|^2 dV)$ [43], where $\Delta\omega$ is change of resonance circular frequency caused by material perturbation, $\Delta\varepsilon$ is the change of material's dielectric permittivity. Increasing of refractive index and permittivity of spacer causes $\Delta\varepsilon > 0$. Thereby, the resonance shifts towards a long wavelength ($\Delta\omega < 0$) according to perturbation theory. Effects of spacers thickness on resonance are shown in Figure 7b, showing that resonance wavelength redshifts from 1537 nm to 1562 nm when the t_1 changes from 30 nm to 46 nm, which may provide a new route to design the resonance wavelength of MPA.

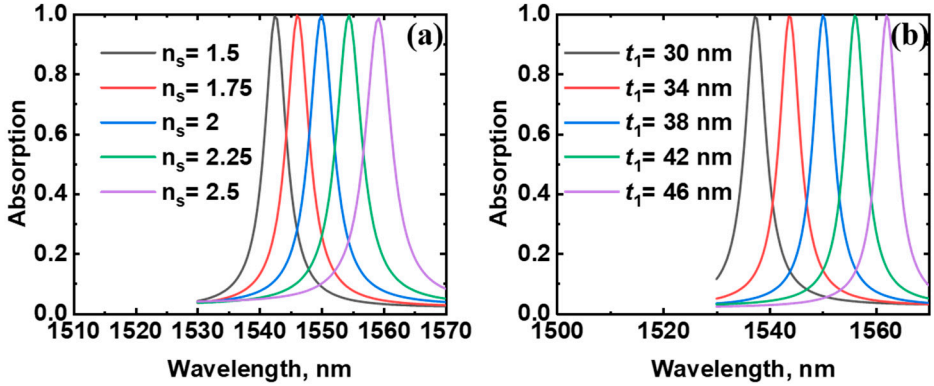

Figure 7. Absorption spectra for changing the spacer's (**a**) refractive index ns and (**b**) thickness t1.

The resonant wavelength of the MPA is dependent on the surrounding background medium, which is promising for air sensing applications. Sensing performance can be evaluated by the following formula with sensitivity S and figure of merit (FOM)

$$S = \frac{\Delta\lambda}{\Delta n}, \text{FOM} = \frac{S}{\text{FWHM}} \tag{14}$$

where $\Delta\lambda$ is the resonance peak wavelength shift and Δn is the refractive index change of the surrounding background medium. As depicted in Figure 8a, increasing the refractive index of the background medium from 1 to 1.05 can cause a red shift of resonance wavelength from 1550 nm to 1561 nm with nearly unchanged FWHM about 5 nm and step interval about 2.2 nm. The slope of the linear fitting line in Figure 8b indicates a sensitivity S = 226 nm/RIU and obtained FOM = 44.1.

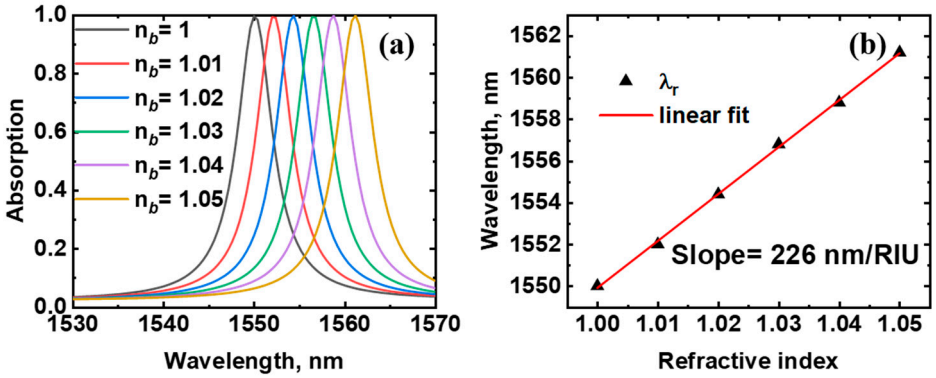

Figure 8. (**a**) Absorption spectra of the MPA with increasing the refractive index of surrounding background medium from 1 to 1.05 with step interval of 0.01. (**b**) Linear fitting of resonant absorption peak wavelength as a function of surrounding background medium's refractive index.

4. Conclusions

In summary, MPA composed of a-Si disk symmetric quadrumer clusters, dielectric spacer, and Au substrate was proposed and the mechanism of the toroidal dipole excitation was analyzed by near field distribution and multipole decomposition of far field scattering powers. Effects of the geometrical parameters on the toroidal dipole resonance absorption were studied. The direction of the toroidal dipole moment can be tuned linearly by changing the polarization angle without weakening the absorption ability. Narrow bandwidth, polarization-independent, and high sensitivity to the refractive index fluctuation of the surrounding background medium may facilitate this metamaterial absorber to be promising in the gas sensing application area.

Author Contributions: Conceptualization, Y.H. and K.Z.; methodology, Y.C.; software and validation, Y.C.; writing-original draft preparation, Y.C.; supervision and project administration, Y.H. and K.Z.; funding acquisition, Y.H. and K.Z. All authors have read and agreed to the published version of the manuscript.

Funding: This work was supported by the National Natural Science Foundation of China (Grant Nos. 52176051 and 51876004) and Fundamental Research Funds for Central Universities (Grant No. YWF-22-L-818).

Institutional Review Board Statement: Not applicable.

Informed Consent Statement: Not applicable.

Data Availability Statement: Not applicable.

Conflicts of Interest: The authors declare no conflict of interest.

References

1. Cui, Y.; He, Y.; Jin, Y.; Ding, F.; Yang, L.; Ye, Y.; Zhong, S.; Lin, Y.; He, S. Plasmonic and Metamaterial Structures as Electromagnetic Absorbers. *Laser Photon. Rev.* **2014**, *8*, 495–520. [CrossRef]
2. Chang, C.-C.; Kort-Kamp, W.J.M.; Nogan, J.; Luk, T.S.; Azad, A.K.; Taylor, A.J.; Dalvit, D.A.R.; Sykora, M.; Chen, H.-T. High-Temperature Refractory Metasurfaces for Solar Thermophotovoltaic Energy Harvesting. *Nano Lett.* **2018**, *18*, 7665–7673. [CrossRef]
3. Silva-Oelker, G.; Jerez-Hanckes, C.; Fay, P. High-Temperature Tungsten-Hafnia Optimized Selective Thermal Emitters for Thermophotovoltaic Applications. *J. Quant. Spectrosc. Radiat. Transf.* **2019**, *231*, 61–68. [CrossRef]
4. Kim, J.; Han, K.; Hahn, J.W. Selective Dual-Band Metamaterial Perfect Absorber for Infrared Stealth Technology. *Sci. Rep.* **2017**, *7*, 6740. [CrossRef]
5. Zhao, L.; Liu, H.; He, Z.; Dong, S. All-Metal Frequency-Selective Absorber/Emitter for Laser Stealth and Infrared Stealth. *Appl. Opt.* **2018**, *57*, 1757. [CrossRef]
6. Raman, A.P.; Anoma, M.A.; Zhu, L.; Rephaeli, E.; Fan, S. Passive Radiative Cooling below Ambient Air Temperature under Direct Sunlight. *Nature* **2014**, *515*, 540–544. [CrossRef]
7. Hervé, A.; Drévillon, J.; Ezzahri, Y.; Joulain, K. Radiative Cooling by Tailoring Surfaces with Microstructures: Association of a Grating and a Multi-Layer Structure. *J. Quant. Spectrosc. Radiat. Transf.* **2018**, *221*, 155–163. [CrossRef]
8. Wang, K.; Hu, H.; Lu, S.; Jin, M.; Wang, Y.; He, T. Visible and Near-Infrared Dual-Band Photodetector Based on Gold–Silicon Metamaterial. *Appl. Phys. Lett.* **2020**, *116*, 203107. [CrossRef]
9. Luxmoore, I.J.; Liu, P.Q.; Li, P.; Faist, J.; Nash, G.R. Graphene–Metamaterial Photodetectors for Integrated Infrared Sensing. *ACS Photonics* **2016**, *3*, 936–941. [CrossRef]
10. Liu, N.; Mesch, M.; Weiss, T.; Hentschel, M.; Giessen, H. Infrared Perfect Absorber and Its Application as Plasmonic Sensor. *Nano Lett.* **2010**, *10*, 2342–2348. [CrossRef]
11. Dănilă, O. Spectroscopic Assessment of a Simple Hybrid Si-Au Cell Metasurface-Based Sensor in the Mid-Infrared Domain. *J. Quant. Spectrosc. Radiat. Transf.* **2020**, *254*, 107209. [CrossRef]
12. Chen, J.; Nie, H.; Tang, C.; Cui, Y.; Yan, B.; Zhang, Z. Highly sensitive refractive-index sensor based on strong magnetic resonance in metamaterials. *Appl. Phys. Express* **2019**, *12*, 052015. [CrossRef]
13. Chen, J.; Peng, C.; Qi, S.; Zhang, Q.; Tang, C.; Shen, X. Photonic Microcavity-Enhanced Magnetic Plasmon Resonance of Metamaterials for Sensing Applications. *IEEE Photonics Technol. Lett.* **2019**, *31*, 113–116. [CrossRef]
14. Zhang, Y.; Feng, Y.; Zhu, B.; Zhao, J.; Jiang, T. Graphene Based Tunable Metamaterial Absorber and Polarization Modulation in Terahertz Frequency. *Opt. Express* **2014**, *22*, 22743. [CrossRef]
15. Chen, J.; Chen, S.; Gu, P.; Yan, Z.; Tang, C.; Xu, Z.; Liu, B.; Liu, Z. Electrically Modulating and Switching Infrared Absorption of Monolayer Graphene in Metamaterials. *Carbon N. Y.* **2020**, *162*, 187–194. [CrossRef]
16. Landy, N.I.; Sajuyigbe, S.; Mock, J.J.; Smith, D.R.; Padilla, W.J. Perfect Metamaterial Absorber. *Phys. Rev. Lett.* **2008**, *100*, 207402. [CrossRef]
17. Ha, D.T.; Tung, B.S.; Khuyen, B.X.; Pham, T.S.; Tung, N.T.; Tung, N.H.; Hoa, N.T.; Lam, V.D.; Zheng, H.; Chen, L.; et al. Dual-Band, Polarization-Insensitive, Ultrathin and Flexible Metamaterial Absorber Based on High-Order Magnetic Resonance. *Photonics* **2021**, *8*, 574. [CrossRef]
18. Yang, C.-Y.; Yang, J.-H.; Yang, Z.-Y.; Zhou, Z.-X.; Sun, M.-G.; Babicheva, V.E.; Chen, K.-P. Nonradiating Silicon Nanoantenna Metasurfaces as Narrowband Absorbers. *ACS Photonics* **2018**, *5*, 2596–2601. [CrossRef]
19. Cai, Y.; Huang, Y.; Zhu, K.; Wu, H. Direction-Independent Dual-Band Perfect Absorption Induced by Fundamental Magnetic Polaritons. *Opt. Express* **2019**, *27*, A1431. [CrossRef]
20. Shamkhi, H.K.; Sayanskiy, A.; Valero, A.C.; Kupriianov, A.S.; Kapitanova, P.; Kivshar, Y.S.; Shalin, A.S.; Tuz, V.R. Transparency and Perfect Absorption of All-Dielectric Resonant Metasurfaces Governed by the Transverse Kerker Effect. *Phys. Rev. Mater.* **2019**, *3*, 085201. [CrossRef]
21. Liang, Y.; Koshelev, K.; Zhang, F.; Lin, H.; Lin, S.; Wu, J. Bound States in the Continuum in Anisotropic Plasmonic Metasurfaces. *Nano Lett.* **2020**, *20*, 6351–6356. [CrossRef]
22. Talebi, N.; Guo, S.; van Aken, P.A. Theory and Applications of Toroidal Moments in Electrodynamics: Their Emergence, Characteristics, and Technological Relevance. *Nanophotonics* **2018**, *7*, 93–110. [CrossRef]
23. Gupta, M.; Singh, R. Toroidal Metasurfaces in a 2D Flatland. *Rev. Phys.* **2020**, *5*, 100040. [CrossRef]
24. Kaelberer, T.; Fedotov, V.A.; Papasimakis, N.; Tsai, D.P.; Zheludev, N.I. Toroidal Dipolar Response in a Metamaterial. *Science* **2010**, *330*, 1510–1512. [CrossRef]
25. Stenishchev, I.V.; Basharin, A.A. Toroidal Response in All-Dielectric Metamaterials Based on Water. *Sci. Rep.* **2017**, *7*, 9468. [CrossRef]
26. Marinov, K.; Boardman, A.D.; Fedotov, V.A.; Zheludev, N. Toroidal Metamaterial. *New J. Phys.* **2007**, *9*, 324. [CrossRef]
27. Huang, Y.-W.; Chen, W.T.; Wu, P.C.; Fedotov, V.; Savinov, V.; Ho, Y.Z.; Chau, Y.-F.; Zheludev, N.I.; Tsai, D.P. Design of Plasmonic Toroidal Metamaterials at Optical Frequencies. *Opt. Express* **2012**, *20*, 1760. [CrossRef]
28. Ögüt, B.; Talebi, N.; Vogelgesang, R.; Sigle, W.; Van Aken, P.A. Toroidal Plasmonic Eigenmodes in Oligomer Nanocavities for the Visible. *Nano Lett.* **2012**, *12*, 5239. [CrossRef]
29. Tang, C.; Yan, B.; Wang, Q.; Chen, J.; Yan, Z.; Liu, F.; Chen, N.; Sui, C. Toroidal Dipolar Excitation in Metamaterials Consisting of Metal Nanodisks and a Dielectrc Spacer on Metal Substrate. *Sci. Rep.* **2017**, *7*, 582. [CrossRef]

30. Fan, Y.; Wei, Z.; Li, H.; Chen, H.; Soukoulis, C.M. Low-Loss and High-Q Planar Metamaterial with Toroidal Moment. *Phys. Rev. B* **2013**, *87*, 115417. [CrossRef]
31. Tuz, V.R.; Khardikov, V.V.; Kivshar, Y.S. All-Dielectric Resonant Metasurfaces with a Strong Toroidal Response. *ACS Photonics* **2018**, *5*, 1871–1876. [CrossRef]
32. Liu, X.; Li, J.; Zhang, Q.; Wang, Y. Dual-Toroidal Dipole Excitation on Permittivity-Asymmetric Dielectric Metasurfaces. *Opt. Lett.* **2020**, *45*, 2826–2829. [CrossRef]
33. Wang, W.; Qi, J. Polarization Sensitive Toroidal Dipole Metasurface for Switch and Magnetic Field Tunability. *Appl. Phys. Express* **2019**, *12*, 065004. [CrossRef]
34. Li, J.; Wang, Y.; Jin, R.; Li, J.; Dong, Z. Toroidal-Dipole Induced Plasmonic Perfect Absorber. *J. Phys. D. Appl. Phys.* **2017**, *50*, 485301. [CrossRef]
35. Li, J.; Zhai, Y.; Li, W.; Cao, Y.; Dong, Z. Perfect Absorption Induced by Plasmon Toriodal Mode for Hot Electron Based NIR Photo-Detection. *Appl. Phys. Express* **2020**, *13*, 122003. [CrossRef]
36. Luo, J.; Lin, Q.; Wang, L.; Xia, S.; Meng, H.; Zhai, X. Ultrasensitive Tunable Terahertz Sensor Based on Five-Band Perfect Absorber with Dirac Semimetal. *Opt. Express* **2019**, *27*, 20165. [CrossRef]
37. Chen, S.; Chen, Z.; Liu, J.; Cheng, J.; Zhou, Y.; Xiao, L.; Chen, K. Ultra-Narrow Band Mid-Infrared Perfect Absorber Based on Hybrid Dielectric Metasurface. *Nanomaterials* **2019**, *9*, 1350. [CrossRef]
38. Wang, L.P.; Basu, S.; Zhang, Z.M. Direct Measurement of Thermal Emission from a Fabry–Perot Cavity Resonator. *J. Heat Transf.* **2012**, *134*, 72701–72709. [CrossRef]
39. Duttagupta, S.; Ma, F.; Hoex, B.; Mueller, T.; Aberle, A.G. Optimised Antireflection Coatings Using Silicon Nitride on Textured Silicon Surfaces Based on Measurements and Multidimensional Modelling. *Energy Procedia* **2012**, *15*, 78–83. [CrossRef]
40. Wu, P.C.; Liao, C.Y.; Savinov, V.; Chung, T.L.; Chen, W.T.; Huang, Y.-W.; Wu, P.R.; Chen, Y.-H.; Liu, A.-Q.; Zheludev, N.I.; et al. Optical Anapole Metamaterial. *ACS Nano* **2018**, *12*, 1920–1927. [CrossRef]
41. Piper, J.R.; Fan, S. Total Absorption in a Graphene Monolayer in the Optical Regime by Critical Coupling with a Photonic Crystal Guided Resonance. *ACS Photonics* **2014**, *1*, 347–353. [CrossRef]
42. Liu, G.-D.; Zhai, X.; Meng, H.-Y.; Lin, Q.; Huang, Y.; Zhao, C.-J.; Wang, L.-L. Dirac Semimetals Based Tunable Narrowband Absorber at Terahertz Frequencies. *Opt. Express* **2018**, *26*, 11471. [CrossRef]
43. Yao, Y.; Kats, M.A.; Genevet, P.; Yu, N.; Song, Y.; Kong, J.; Capasso, F. Broad Electrical Tuning of Graphene-Loaded Plasmonic Antennas. *Nano Lett.* **2013**, *13*, 1257–1264. [CrossRef]
44. Wang, J.; Yang, J.; Shi, D. Perfect Absorption for Monolayer Transition-Metal Dichalcogenides by Critical Coupling. *Nanotechnology* **2020**, *31*, 465205. [CrossRef]
45. Xiang, J.; Xu, Y.; Chen, J.-D.; Lan, S. Tailoring the Spatial Localization of Bound State in the Continuum in Plasmonic-Dielectric Hybrid System. *Nanophotonics* **2020**, *9*, 133–142. [CrossRef]